geosciences

MDPI

Article

Fluid Redox Fingerprint of the $CaCO_3$+Antigorite Dehydration Reaction in Subducted Metacarbonate Sediments

Andrea Maffeis [1,*], Simona Ferrando [1,*], James Alexander Denis Connolly [2], Maria Luce Frezzotti [3] and Daniele Castelli [1]

[1] Dipartimento di Scienze della Terra, Università degli Studi di Torino, 10125 Turin, Italy
[2] Institute for Geochemistry and Petrology, Department of Earth Sciences, ETH Zurich, CH 8092 Zurich, Switzerland
[3] Dipartimento di Scienze dell'Ambiente e della Terra, Università degli Studi di Milano-Bicocca, 20126 Milano, Italy
* Correspondence: andrea.maffeis@unito.it (A.M.); simona.ferrando@unito.it (S.F.)

Abstract: Antigorite dehydration is a process able to release, in comparison with other minerals, the highest amount of H_2O from a subducting slab. The released fluid delivers critical elements (e.g., S, Cu, and REE) to the overlying subarc mantle, modifying the mantle source of arc magmas and related ore deposits. Whether antigorite breakdown produces oxidising or reducing fluids is debated. Whereas previous studies have investigated antigorite dehydration in serpentinites (i.e., in a (C)AMFS-H_2O system), this contribution is devoted to the CMFS-COHS carbonate system, which is representative of the metacarbonate sediments (or carbonate-dominated ophicarbonate rocks) that sit atop the slab. Thermodynamic modelling is used to investigate the redox effect of the carbonate-buffered antigorite dehydration reactions (i.e., brucite breakdown and antigorite breakdown) on electrolytic fluid geochemistry as a function of *P*-*T*-fO_2. The influence of *P*-*T*-fO_2 conditions on the solubility of C and S, solute-bound H_2 and O_2, fluid pH, the average valence states of dissolved C and S, and the fluid redox budget indicates that, in metacarbonate sediments, the $CaCO_3$+antigorite reaction tends to produce reducing fluids. However, the redox state of such fluids is buffered not only by the redox state of the system but also, most importantly, by concomitantly dissolving redox-sensitive minerals (i.e., carbonates, graphite, pyrite, and anhydrite). A qualitative correlation between the redox state of the system and the possible depth of fluid release into the mantle wedge is also derived.

Keywords: antigorite dehydration; redox; thermodynamic modelling; electrolytic fluid; redox budget; subduction; metacarbonate sediments; subduction zone fluids; carbon; sulfur

Citation: Maffeis, A.; Ferrando, S.; Connolly, J.A.D.; Frezzotti, M.L.; Castelli, D. Fluid Redox Fingerprint of the $CaCO_3$+Antigorite Dehydration Reaction in Subducted Metacarbonate Sediments. *Geosciences* **2023**, *13*, 130. https://doi.org/10.3390/geosciences13050130

Academic Editors: Markes E. Johnson and Jesus Martinez-Frias

Received: 20 December 2022
Revised: 22 April 2023
Accepted: 27 April 2023
Published: 30 April 2023

1. Introduction

The subarc mantle is more oxidised than the surrounding subcontinental or suboceanic mantle (e.g., [1,2]). This trait dictates mantle melting behaviour and, consequently, the physicochemical properties of the resulting liquids and the related extraction of the critical elements (Cu, Mo, Au, and REE; [3,4]) necessary for ore-forming processes within the arc crust. The mantle wedge's metasomatism and oxidation are thought to be caused by slab-derived fluids that deliver oxidising redox-sensitive elements, such as O, H, S, C, Fe, and N.

Antigorite breakdown is the most significant dehydration event that occurs in the subducting slab at forearc-to-subarc depths. Antigorite is the dominant constituent of subducted serpentinites and ophicarbonates, and it is also common in the impure marbles derived from metamorphism and the hydration of dolostones (e.g., [5]; Figure 1a). Antigorite dehydration is under scrutiny from the petrologic community due to its ambiguous role in influencing the geochemistry and, most importantly, the redox of fluids that interact with the mantle wedge [6–17]. More specifically, different views are reported in the

literature, stemming from the different strategies adopted for investigating this petrologic process, i.e., direct observations from the study of natural samples or indirect observations from experiments or thermodynamic modelling. Ultimately, three different views can be recognised:

I. Antigorite breakdown produces oxidising fluids [7,8,11,13,15–17], thus straightforwardly explaining mantle wedge oxidation;
II. Antigorite breakdown releases reducing fluids [6,9,10], implying that mantle wedge oxidation is either apparent or requires other processes to be explained;
III. Antigorite breakdown produces either reducing or oxidising fluid (since it spans roughly 8–9 log fO_2 [12,16], from a reduced −5 to an oxidised +4 Δlog fO_2 units with respect to the Fayalite–Magnetite–Quartz oxygen buffer, FMQ), depending on the *P-T* path experienced by the subducted rocks [12] or on the pre-subduction redox state of the system [14].

All these studies investigate antigorite dehydration in serpentinites, i.e., in a (C)AMFS-H_2O system. Interestingly, a recent experimental investigation [15] of carbonate-rich (up to 20 wt%) serpentinites highlights how graphite and, more markedly, $CaCO_3$ decrease the *P-T* conditions of antigorite destabilisation. Thus, this paper reveals that C is important for the metamorphic and redox evolution of antigorite-bearing rocks during subduction. Notably, such a role of C in modulating serpentinite redox evolution has been contemporaneously confirmed by field observations in the Monviso meta-ophiolite [16]. Moreover, most of the above studies investigated antigorite dehydration as a process producing OH or COH fluids, and only a few studies explored the release of SOH fluids [9,10,13,14], while none took into account the production of solute-bearing COHS fluids.

In this work, we model the *P-T-f*O_2 evolution of an impure carbonatic system (i.e., the CM(F)S-COHS system) by using the electrolytic fluid thermodynamic approach. This work aims to investigate the redox state not only of the dehydration reactions involving antigorite (i.e., brucite and antigorite breakdown) but also of the produced COHS fluid under carbonate-buffered conditions.

Thermodynamic modelling was applied to an ultra-high pressure (UH*P*) impure marble from the Brossasco-Isasca Unit (BIU) of the Dora-Maira Massif (Italian Western Alps). Because of the mineralogy of such marble (i.e., calcite, dolomite, diopside, forsterite with minor tremolite, antigorite, talc, and brucite), its phase relations during metamorphism are similar to those of the classic ultramafic system represented by serpentinites; however, the presence of carbonates also makes the studied system interesting for application to ophicarbonate rocks (e.g., [5]). The refractory nature of Fe when being mobilised by aqueous fluids under metamorphic conditions diminishes the impact of its low amounts in the studied system on the resulting fluid chemistry (e.g., [18,19]). In addition to this, the lack of Fe allows for the decoupling of its potential influence in buffering the fO_2 evolution of the antigorite dehydration reaction in carbonate-buffered systems.

The investigated *P-T* conditions are those of the prograde path of the BIU (see the recent compilation of [20,21]) because (i) we can compare the results from the thermodynamic modelling with the mineral and fluid data available from the natural sample DM675 (see below), and (ii) this *P-T* path can be considered representative of the *P-T* evolution of the slab in cold subductions (e.g., [22]).

2. Geological and Petrological Setting

The investigated metasedimentary rock has been sampled from the Costa Monforte marble lens of the UHP Brossasco-Isasca Unit of the Dora-Maira Massif (e.g., [23–25]). The Alpine polyphasic *P-T*-t evolution of this unit has been determined through 40 years of multiple petrologic studies on several lithologies (see [20,21] for a review).

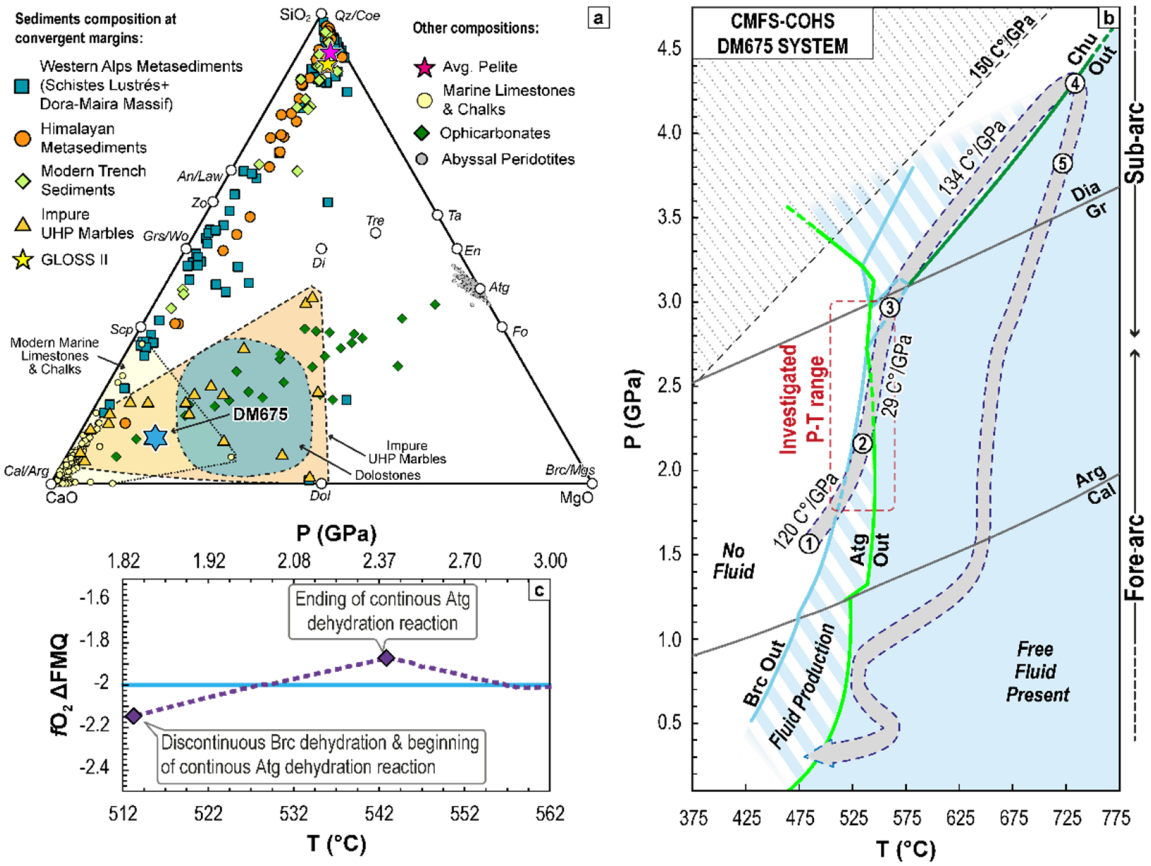

Figure 1. (**a**) Comparison between DM675 bulk composition ([26]; Table 1) and other subducted carbonate and carbonate-bearing metasediments from the Western Alps [27–30], Himalaya [31], modern trench sediments and GLOSS II [32], and other UHP localities (i.e., Sulu, Thiashan, Kokchetav; [33–35]). In addition, modern marine limestones and chalk are shown (see compilation in [36,37]). The average pelite composition is from [38]. Ophicarbonates are compiled from [39,40], and the abyssal peridotites are from [41]. All compositions are calculated as volatile-free and as mol%. (**b**) BIU *P-T* path from [20,21]; the red box highlights the investigated *P-T* range. The portrayed phase relationships are from the DM675 isochemical phase diagram in [26]. (**c**) $T(P)$ $-fO_2$ evolution of sample DM675 in the investigated *P-T* range using the oxygen chemical potentials, calculated along the prograde BIU *P-T* path, from the *P-T* DM675 isochemical phase diagram in [26].

The prominent petrologic and tectonic processes that occurred in the Brossasco-Isasca Unit during the investigated prograde to early-retrograde evolution are (numbers refer to those reported in Figure 1b) as follows: (1) a prograde stage at 450–570 °C and 1.0–1.8 GPa; (2) prograde dehydration reactions and intense Mg-metasomatism along shear zones at 520–540 °C and 1.6–2.3 GPa; (3) the development of a prograde foliation coupled with dehydration reactions, with multiple carbonate dissolution–precipitation events in marbles and local Mg-metasomatism in metagranitoids, at 540–560 °C and ca. 2.5–3.0 GPa (i.e., at the quartz–coesite transition); (4) UHP peak and low dehydration at ca. 730 °C and 4.3 GPa and dated at ca. 35 Ma; and (5) the development of the UHP main regional foliation during early, nearly isothermal, decompression at ca. 720–740 °C and 3.7–4.0 GPa [20,21,42–48].

The sample DM675 is a UHP impure calcitic–dolomitic marble composed of calcite (after former aragonite), dolomite, forsterite, and diopside. Its bulk composition (Table 1) is located along a chemical trend that joins the (hydrated) abyssal peridotites (i.e., the (C)MFS$-H_2O$ sub-system) to the marine limestones and chalks (i.e., the CM(F)(S)-COHS sub-system), and it is compatible with some carbonate-rich ophicarbonates (Figure 1a). The investigated sample records multiple carbonate dissolution–precipitation events during its HP−UHP prograde dehydration (Ferrando et al. [20]; Maffeis et al. [26]). The composition

of the released fluid was a solute-bearing aqueous fluid, i.e., a fluid poor in Cl and in non-polar molecular species (such as CO_2, CH_4, and N_2) but containing a dissolved load, ranging from a few percent up to 11 wt%, of other charged ions or neutral species (i.e., Si, Ca, Mg, Fe, C, S, O, and H; [26]).

Table 1. Bulk-rock composition of marble DM675 used in the calculations, as obtained by Maffeis et al. [26]. The "oxidised" version of the DM675 bulk composition is obtained from the "starting" one by increasing only the O_2 in order to stabilise anhydrite. The "oxidised" version of the DM675 is only used for *P-T* phase diagram calculation in the Discussion Section (Section 5.4).

	Used (reduced) DM675 El mol	Oxidised DM675 El mol
Si	3.0186	3.0186
Fe^{2+}	0.1171	0.1171
Mg	4.5242	4.5242
Ca	23.5540	23.5540
H_2	2.7526	2.7526
C	23.5337	23.5337
S_2	0.0604	0.0604
O_2	41.7392	42.1649

3. Methods

Phase diagram sections ($T(P)$ $-fO_2$; Figure 2) were calculated using Perple_X software (version 6.9.1; [49,50]) for the Ca−Mg−Fe−Si−C−O_2−S_2−H_2 (CM(F)S-COHS) chemical system, modelling part of the prograde BIU *P-T* path, between 512 and 562 °C and between 1.82 and 3.00 GPa (Figure 1b; Supplementary Table S1). Compositional phase diagrams were calculated with the "Lagged Speciation" algorithm [50], with condensed phase and molecular volatile species data from Holland and Powell ([51] revised 2018, version DS6.22) and solute species data from the DEW/HKF model of Sverjensky et al. ([52], revised 2017). For these calculations, the solvent consisted of a mixture of H_2O, CO_2, CH_4, H_2S, and C_2H_6. In particular, C_2H_6 was added to the solvent to be used as a control for the molecular fluid model to check the reliability of hydrocarbons (heavier than methane) calculated via electrolytic fluid models in the fluid phase. CO and SO_2 were treated as solute species due to their low molar abundance in exploratory calculations. The Pitzer and Sterner [53] EoS was used to describe pure H_2O and CO_2; all other pure fluid properties were computed from the Redlich–Kwong EoS, and the Modified Redlich–Kwong (MRK) EoS of de Santis et al. [54] was used to compute the activities of all solvent species. To model the fluid solute composition and speciation, all fluid species were considered, except for those that replicate solvent species. The selected mineral pure phases were quartz, coesite, chondrodite, pyrite, graphite, and diamond. The used solution models were Holland and Powell [55] for olivine and clinopyroxene; Padrón-Navarta et al. [56] for antigorite; Evans et al. [57] for pyrrhotite; Anovitz and Essene [58] for calcite (and aragonite) and dolomite; the ideal solution model for talc, tremolite, Phase-A, and clinohumite; and the simplicial solution model for periclase.

As explained in a previous paper (i.e., [26]), the used DM675 bulk-rock composition (Table 1) was adjusted for O_2 content until it reproduced the observed microstructures, the presence of graphite as solid inclusions, and the composition of the fluid trapped within prograde-to-peak clinopyroxene as fluid inclusions [20,26].

The obtained bulk composition and *P-T* isochemical phase diagram were used to estimate the DM675 fO_2 as a function of *P* and *T* along the prograde *P-T* path of the BIU. The DM675's $fO_2^{T,P}$ was calculated using the DM675 μO_2 sampled along the prograde BIU

P-T path ($\mu O_{2ROCK}^{T,P}$) in the *P-T* isochemical phase diagram—calculated using electrolytic fluid models (Supplementary Figure S4 of [24])—and used in the following equation:

$$fO_2^{T,P} = \exp \frac{\mu O_{2ROCK}^{T,P} - \mu O_{2PURE}^{T,1bar}}{RT}$$

where $\mu O_{2PURE}^{T,1bar}$ is the chemical potential of pure oxygen calculated between 487 °C and 730 °C at 1 bar with Perple_X (FRENDLY subprogram) using the condensed phase and molecular volatile species data from Holland and Powell ([51] revised 2018, version DS6.22) and solute species data from the DEW/HKF model of (Sverjensky et al. [52], revised 2017). R is the gas constant (8.31446261815324 J/K mol). The position of the Fayalite–Quartz–Magnetite (FMQ) oxygen buffer ([59]; yellow line in Figure 2) was calculated as a univariant equilibrium, i.e., as *T(P)*-fO_2 Schreinemaker projections along the same *P-T* path used for the *T*(*P*) $-fO_2$ isochemical phase diagrams. Perple_X software (version 6.9.1; [49,50]) was used with the condensed phase and molecular volatile species data from Holland and Powell ([51] revised 2018, version DS6.22).

To evaluate the redox capacity of the fluid produced by the investigated system, a specific redox variable related to the sample's electron availability has to be used [60]. The redox budget (RB) is the product of the amount of redox-sensitive elements *E* (n_E) and the number of electrons necessary to either oxidise or reduce a given element (at a starting valence state v_{sample}) to another (*reference*) valence state ($v_{reference}$; [60]):

$$RB = \Sigma n_E v_i = \Sigma n_E \left(v_{sample} - v_{reference} \right)$$

The RB, which is expressed as moles, can also be used in terms of the unit of mass, and it is called the "specific redox budget" [61]; it is better suited to evaluate the fluxes of redox capacity carried by a fluid. In this study, the RB of the fluid is expressed as the "specific redox budget" (i.e., as the mol of the RB per kg of fluid: mol e^-/kg_{fluid}). The conversion from the redox budget to the "specific redox budget" was accomplished with the following passages:

$$\begin{gathered} E(mol) \cdot molar\ weight\ E\left(\tfrac{g}{mol}\right) = E(g) \\ \left[\frac{E(g)}{\sum E_{fluid}(g)}\right] \cdot 1000 = E\left(\frac{g}{kg_{fluid}}\right) \\ \left[\frac{E(g)}{\sum E_{fluid}(g)}\right] \cdot 1000 = E\left(\frac{g}{kg_{fluid}}\right) \\ E\left(\frac{mol}{kg_{fluid}}\right) \cdot \left(v_{sample} - v_{reference}\right) = RB\left(\frac{e^- mol}{kg_{fluid}}\right) \end{gathered}$$

Sulfur RB was calculated for atomic S and not diatomic S_2. The mineral abbreviations are after [62].

4. Results

4.1. P-T-fO$_2$ Mineral Phase Relationships during CaCO$_3$+ Antigorite Dehydration Reaction

To investigate the role of the $CaCO_3$+antigorite dehydration reactions in influencing the redox state of the released fluid, the system's pressure, temperature, and oxygen fugacity (fO_2) have to be monitored. fO_2 is an intensive variable, expressed as log units of fO_2, commonly used in petrology to investigate the redox character of an investigated system. To moderate the dependence of fO_2 on *P* and *T*, fO_2 values are usually expressed as a deviation from the fO_2 of a reference buffer under the same *P-T* conditions. The most commonly used buffer is Fayalite–Magnetite–Quartz (FMQ). Thus, in the present work, fO_2 is expressed as values of ΔFMQ, with positive values referring to oxidised conditions and negative values indicating reduced conditions, both relative to the FMQ.

For the BIU impure marble DM675, the calculated redox state changes under varying *P-T* conditions (Figure 1c). At 512 °C and 1.82 GPa, the redox state is at ΔFMQ−2.15; it increases to a maximum of ΔFMQ−1.87 at 543 °C and 2.39 GPa, and then it decreases to ΔFMQ−2.01 at 559 °C and 2.91 GPa. These negative values indicate that the sample DM675 is a reduced impure marble.

Using the DM675 as a natural proxy, the equilibrium phase relations (Figure 2) and fluid chemistry for the corresponding CM(F)S–COHS system were modelled along the prograde BIU *P-T* path in the ranges of 1.82–3.00 GPa and 512–562 °C (Figure 1b), as well as in an fO_2 range relevant for monitoring the $CaCO_3$-buffered reaction at redox states between ΔFMQ+2 and ΔFMQ−2.

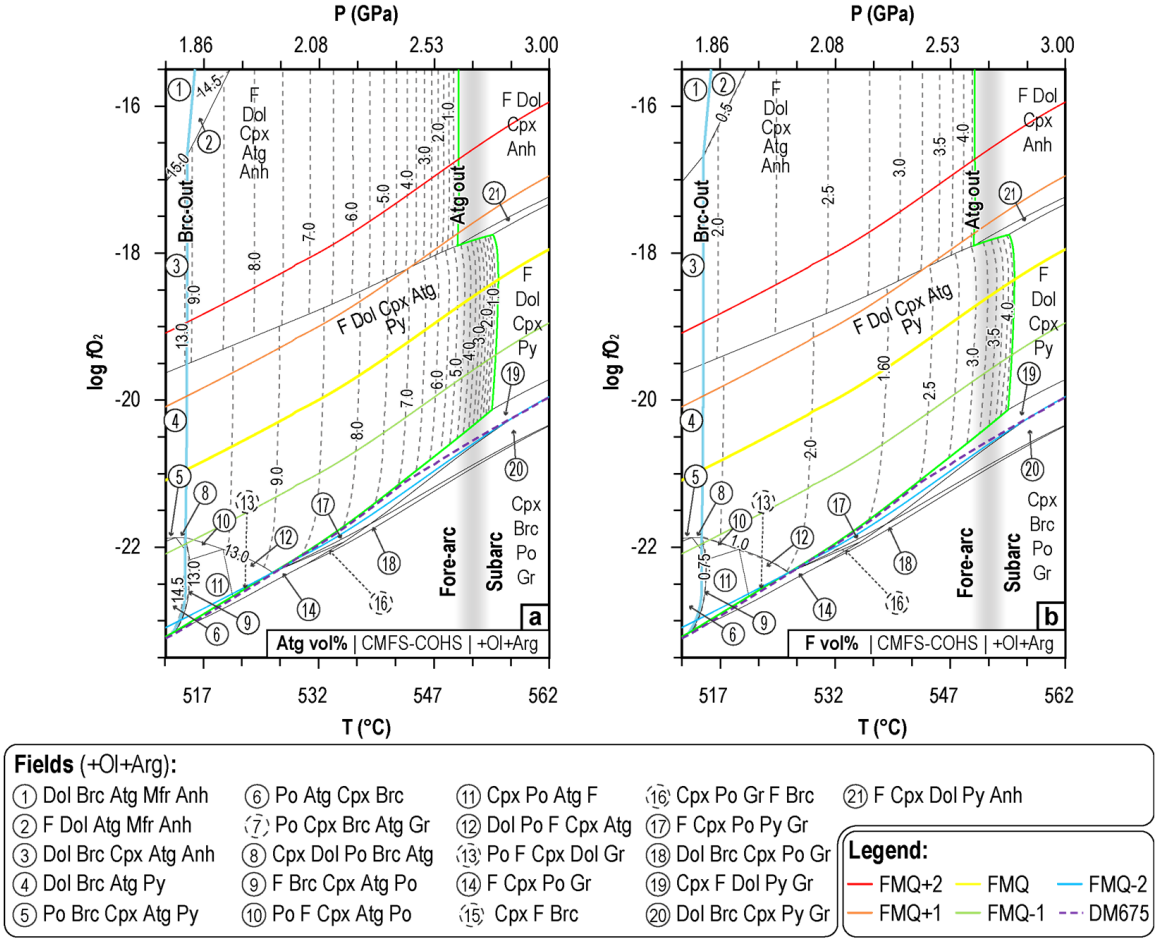

Figure 2. $T(P)$ $-fO_2$ phase diagram calculated for the Atg dehydration reaction. Isomodes showing the variation of Atg vol% (**a**) and fluid (F) vol% (**b**) in the system during reactions α and β. The DM675 $T(P)$ $-fO_2$ path is the same as that plotted in Figure 1b.

The antigorite dehydration reactions are the two major reactions controlling fluid production in the modelled CM(F)S-COHS system as *T* and *P* increase, i.e., during deep subduction (Figures 1b and 2). The first reaction is the discontinuous (univariant) brucite-breakdown reaction that involves the dehydration of both brucite and antigorite, without carbonates involved, up to complete brucite consumption (brucite-out):

$$Brc + Atg \rightarrow Ol + F \cdot (\alpha)$$

The second reaction is the continuous antigorite-breakdown reaction that starts as soon as reaction α is completed and that progressively consumes antigorite up to its whole destabilisation (antigorite-out; Figure 2a):

$$Arg + Atg + \rightarrow Ol + Do + Di + F(+Gr\ only\ at\ \text{FMQ} \lesssim -1.7) \cdot (\beta)$$

While the *P-T* conditions of the brucite breakdown are not influenced by the redox conditions of the system (514 °C and 1.8 GPa; Figures 1b and 2), those of the antigorite breakdown are moderately influenced. Above ΔFMQ+0.7 conditions, complete antigorite consumption occurs at constant *T* and *P* (550 °C and 2.64 GPa, respectively). These *P-T* values are lower than those (555 °C and 2.80 GPa) under redox conditions between ΔFMQ+0.7 and ΔFMQ−1.7. Below ΔFMQ−2, antigorite is substituted by brucite as the major hydrous phase of the system. Under such *P-T*−fO_2 conditions, the topology of the boundary between the antigorite-bearing and antigorite-free fields becomes almost parallel to that of ΔFMQ−2.

As shown in Figure 2, aragonite and dolomite are always stable under the investigated conditions. On the contrary, graphite is stabilised under reduced conditions, below ΔFMQ-1.7. Regarding sulfur-bearing phases, anhydrite substitutes pyrite under oxidised conditions between ΔFMQ+1.5 and ΔFMQ+0.5. Because the modelled bulk composition is Fe-poor, the predicted silicates (Mg-rich olivine, Mg-rich clinopyroxene, antigorite, and brucite) do not play any significant role in buffering oxygen fugacity by hosting potential Fe^{3+}. Instead, carbon-bearing minerals (carbonate and graphite) and sulfur-bearing minerals (sulphates and sulphides) are the solid phases that primarily control the oxygen-buffering capacity of the system.

4.2. P-T-fO_2 Fluid Phase Relationships during $CaCO_3$+Antigorite Dehydration Reactions

As prograde dehydration reactions under high-pressure conditions produce fluids during subduction, the mineral dissolution of the surrounding rock-forming minerals (e.g., [63]) progressively changes the fluid chemistry (e.g., [64]). To better understand how the dissolution process influences the redox state of the resulting fluid, it is essential to evaluate the variations of the dissolved redox-sensitive elements, the average valence state of C and S, and the variations of the fluid pH during prograde mineral dehydration and rock dissolution in the fluid.

4.2.1. Variation of Dissolved Redox-Sensitive Elements

During reaction α, ca. 1.7–2 vol% of fluid, equivalent to 4–4.5 mol% of H_2O, is instantaneously produced above ΔFMQ−2. In contrast, only 0.86 vol% (equivalent to 2 mol% of H_2O) is produced at ΔFMQ−2, and up to 2.54 vol% (equivalent to 5.7 mol% of H_2O) is produced in the DM675 (Figures 2b and 3a). The remaining fluid is produced during reaction β, reaching 4.25–4.50 vol% (corresponding to 9.5 mol% of H_2O) at antigorite-out regardless of the redox conditions (Figures 2b and 3a). The concomitant mineral dissolution gradually decreases the H_2O content in the fluid. Because of the redox-neutral character of H_2O (e.g., [65]), any redox capacity held by the fluid is due to the dissolved element load.

As dehydration reactions proceed, the produced fluid is characterised by an increase in the solute load that can reach up to 8 wt% under oxidised conditions (Figure 3b). The amount of solute is due to the progressive dissolution of carbonate minerals and anhydrite under oxidised conditions or carbonate and sulphides (pyrrhotine and, then, pyrite) under more reduced conditions (Figure 2). These minerals exert primary control on the solute composition, especially on the redox-sensitive elements H, O, C, S, and Fe.

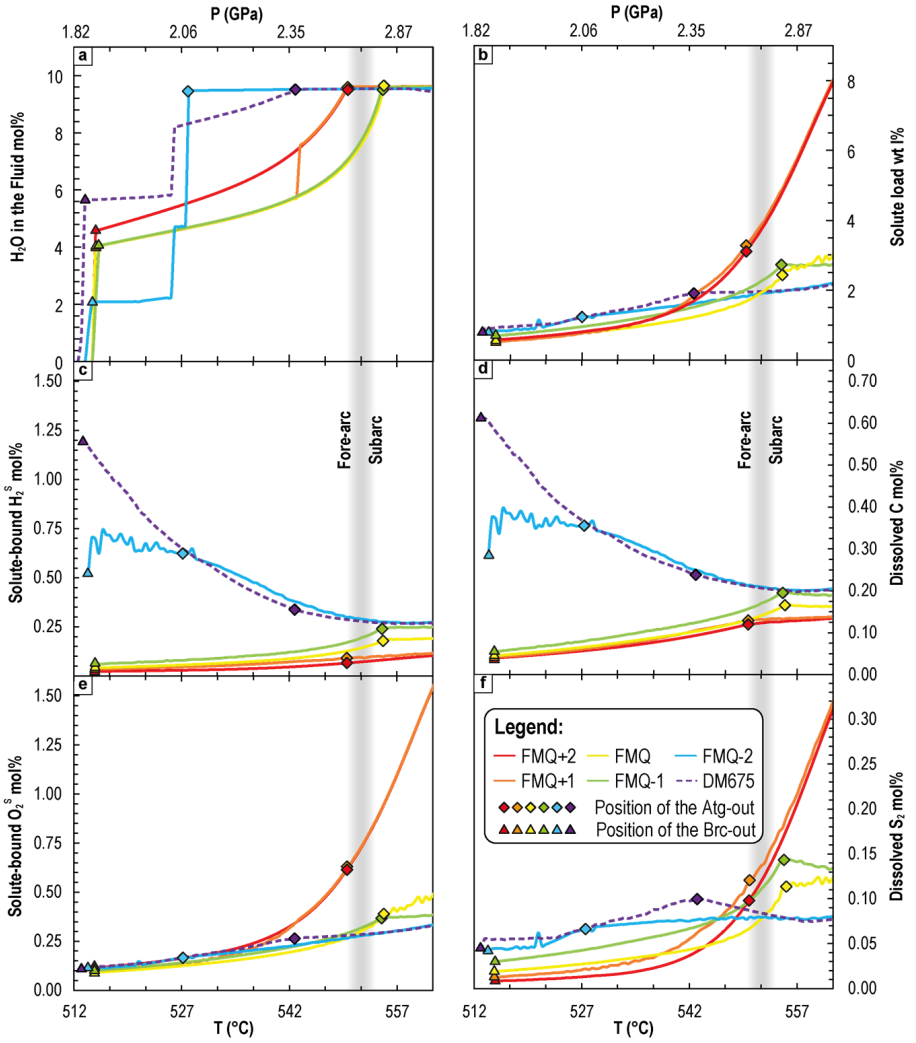

Figure 3. (**a**) Amount of solvent H_2O as mol% constituting the fluid (composed of solvent and solutes) as a function of *P*, *T*, and fO_2. (**b**) Evolution of total dissolved load (wt%) as a function of *P*, *T*, and fO_2. (**c**,**e**) Molar variation of $H_2{}^S$ and $O_2{}^S$ bound to solute and not to H_2O as a function of *T*, *P*, and fO_2. (**d**,**f**) Dissolved C and S_2 in the fluid phase as a function of *T*, *P*, and fO_2.

In particular, the amount of hydrogen and oxygen not bound to H_2O can be considered to explore whether a bulk-fluid composition has a more reducing or oxidising character. Hydrogen and oxygen can also constitute gaseous phases (H_2 and O_2) or can be bound to solutes ($H_2{}^S$ and $O_2{}^S$; from here forward, the superscript "^{S}" is used to refer to the amount of H_2 and O_2 constituting the fluid phase that is bound to the solute portion of the fluid). The $H_2{}^S$ and $O_2{}^S$ abundance in the fluid (Figure 3c,e) is controlled by reactions α and β and by the progressive dissociation of the produced H_2O to H^+ and HO^-. Thus, any variations in $H_2{}^S$ and $O_2{}^S$ are due to the redox behaviour of the reactions themselves. From oxidised to reduced conditions (from ΔFMQ+2 to ΔFMQ−1), the $H_2{}^S$ in the fluid progressively increases during reaction β (Figure 3c). Conversely, at ΔFMQ−2 during reaction α, the amount of $H_2{}^S$ is the highest, and it is progressively diluted by reaction β. On the contrary, the amounts of $O_2{}^S$ are not affected by the redox state of the system but progressively increase as the reactions proceed, particularly under oxidised conditions (Figure 3e).

The amount of dissolved C during reaction β follows the same pattern shown by $H_2{}^S$ (Figure 3d). This similarity is due to the stabilisation of hydrocarbons (especially CH_4) under reduced conditions (derived by dissolving carbonates and graphite) and to dominant $HCO_3{}^-$ species under the other conditions (derived by dissolving carbonates). Sulfur dissolution shows an evolution similar to that of $O_2{}^S$. Dissolved sulfur increases

under oxidised conditions as *P* and *T* increase along a cold subduction *P-T* path (Figure 3f). Correspondingly, sulfur is more soluble under reduced conditions (and at forearc depths, i.e., <2.5 GPa) than under oxidised conditions along a cold subduction *P-T* path (Figure 3f).

Iron is in such low quantities in the studied system that, as shown by Maffeis et al. [26], its limited dissolution leads to an abysmal dissolved load irrelevant for the *P-T-f*O_2 of the system. The highest amounts of dissolved Fe (1.5×10^{-5} and 4×10^{-5} mol%) are released in the fluid during reaction α. As reaction β proceeds, Fe is diluted up to 0.5×10^{-5} mol% (Supplementary Figure S1).

4.2.2. Variation of the Dissolved Average Valence State of C and S

The evaluation of the AVS, i.e., the average valence state of an element, with multiple valence states potentially present at the same time in a fluid, allows for an understanding of the potential redox role of the modelled fluid in the case where it leaves the system and interacts, for example, with an overlying mantle wedge.

The AVS of carbon under oxidised and neutral conditions is substantially constant under all *P-T* conditions (around ~+3.99–+3.96; Figure 4a). At ΔFMQ−1, carbon AVS progressively increases, during reaction β, from +3.50 up to ~+3.86, and then it remains constant. Interestingly, carbon AVS records a considerable change in behaviour when the system is at ΔFMQ−2 (and in the DM675 redox state). As reaction α ends and reaction β takes place, carbon AVS is very low (between −3.20 and −2.20), but it progressively increases up to +2 at the end of the investigated *P-T* portion of the path (Figure 4a).

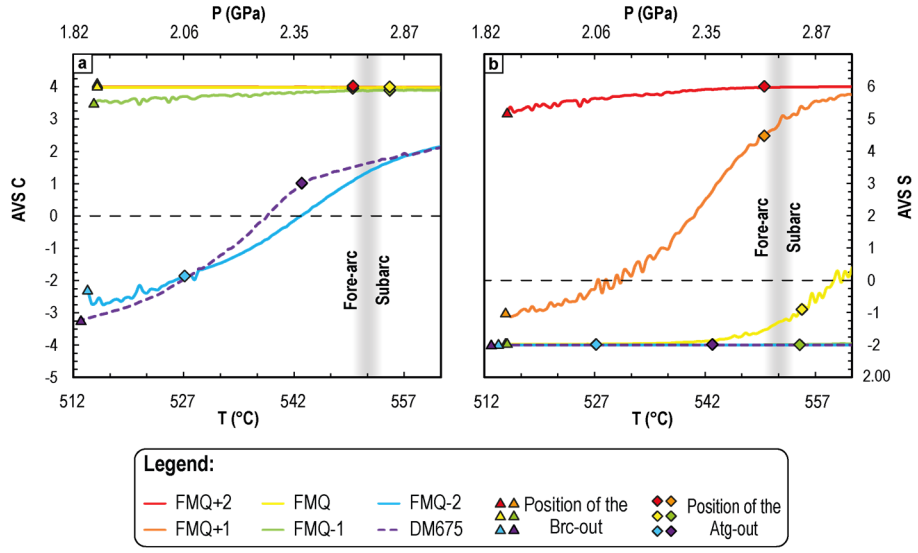

Figure 4. (**a**) Average valence state (AVS) of C dissolved in the fluid as a function of *T*, *P*, and fO_2. (**b**) Average valence state (AVS) of S dissolved in the fluid as a function of *T*, *P*, and fO_2.

Sulfur AVS shows the opposite behaviour with respect to C. At ΔFMQ+2, even though anhydrite dissolves, the starting sulfur AVS is at ~+5.50. It reaches +6 only when antigorite is completely consumed (Figure 4b). A more extreme behaviour is observed at ΔFMQ+1 because pyrite is present under lower *P-T* conditions and anhydrite is present under higher *P-T* conditions (Figure 2). If pyrite is stable in the system (see ΔFMQ+1 path in Figure 2), its dissolution during reaction α and part of reaction β leads to a sulfur AVS of ~−1.10. As anhydrite is stabilised in the rock matrix, sulfur AVS progressively increases up to ~+5.8 at the end of the investigated *P-T* conditions (Figure 4b). Under the neutral and reduced conditions of the system, sulfur AVS remains constant at ~−1.98 within the whole prograde path, due to continuous pyrite dissolution (Figure 4b). However, under neutral conditions, the AVS of sulfur starts to increase near the end of reaction β, reaching ~+0.25 at the end of the investigated *P-T* conditions (Figure 4b).

4.2.3. Variation of the Fluid pH

Since the pH is representative of the activity of the ions H^+ (aH^+) in the fluid, this value is indicative of the modifications of both the H_2O activity and its ionisation constant (i.e., the equilibrium constant, which is dependent on the *P-T* conditions of the system and controls the auto-ionisation or auto-dissociation reaction of H_2O to produce H^+ and OH^-; e.g., [66,67]). Both are linked to changes in the solvent capacity of the fluid. In Figure 5a, it seems that, while both reactions α and β occur, the fluid pH continues to decrease until complete antigorite consumption and then roughly remains stable for the rest of the prograde *P-T* path. However, due to the decrease in the neutral pH ($pH_{NEUTRAL}$) value with increasing *T* and *P* (dashed light blue curve in the inset of Figure 5a), the calculated pH of the fluid is not truly indicative of the changes in the fluid solvent capacity (i.e., it is not directly known whether the fluid becomes more acidic or basic under changing *P-T-f*O_2 conditions). Therefore, to better understand the changes in the solvent ability of H_2O, the pH variation relative to neutrality ($\Delta pH = pH - pH_{NEUTRAL}$; [66,68]) is more informative (Figure 5b,c). The fluid is acidic if $\Delta pH < 0$, and it is alkaline if $\Delta pH > 0$. The positive ΔpH values ($\Delta pH = 1.90 - 1.55$) indicate that the produced fluid is always alkaline, but under reduced conditions, the fluid is more acidic than under oxidised conditions.

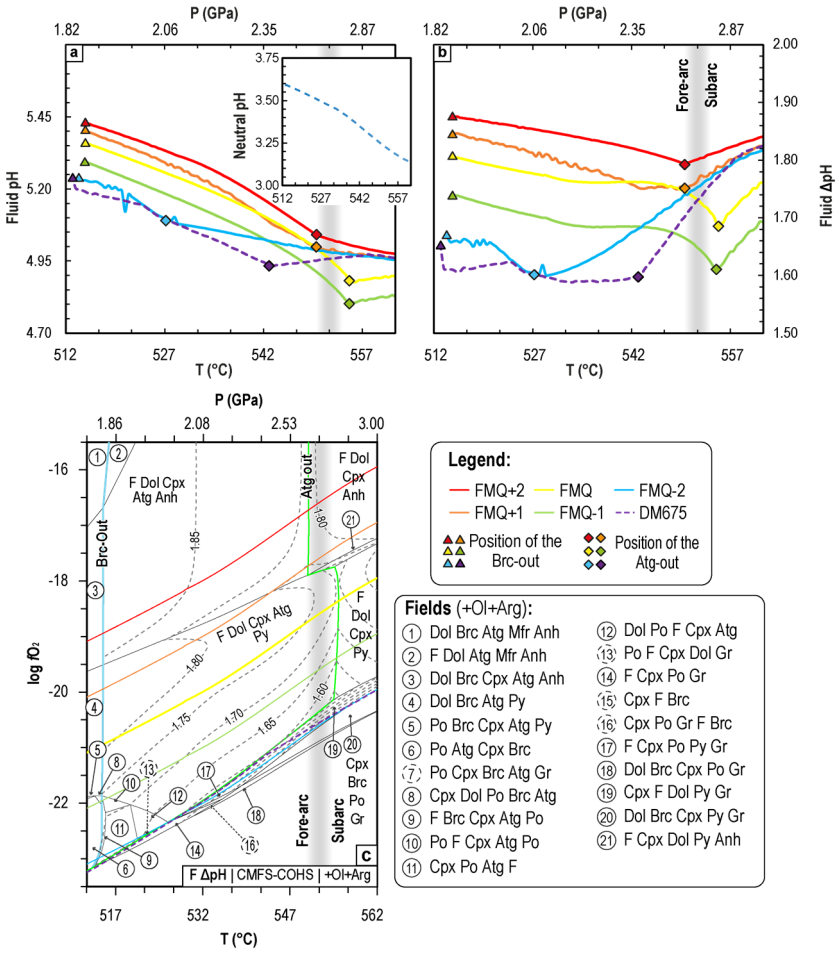

Figure 5. (**a**) Fluid pH as a function of *T*, *P*, and fO_2 with the neutral pH under the *P-T* conditions given in the inset. (**b**) $\Delta pH = pH - pH_{NEUTRAL}$ variation as a function of *T*, *P*, and fO_2. (**c**) Variation of the fluid $\Delta pH = pH - pH_{NEUTRAL}$, first showing a progressive increase in fluid acidity, marked by a decrease in ΔpH values, during the entire $CaCO_3$-buffered antigorite dehydration followed by an abrupt decrease in fluid acidity, marked by an increase in ΔpH values, after the complete consumption of antigorite (bright light green line). Field numbers in the dashed circles are univariant reactions separating the bivariant fields.

5. Discussion

5.1. Redox-Dependent Fluid Chemistry

The preferential release of H_2^S (under progressively more reducing conditions) over O_2^S at all the examined system's redox states is better visualised with the X(O) (X(O) = (O_2^S/(O_2^S + H_2^S)), following [65]) molar ratio of the fluid's dissolved load (Figure 6a). The threshold value of X(O) = 1/3 is that of H_2O and represents the boundary between the oxidising and reducing fluids (following the definition of redox-neutral fluid in [65]) of the solutes in the investigated *P*-*T*-fO_2 range (Figure 6a). Starting from ΔFMQ+2 down to ΔFMQ−1, the value of the ratio shifts downward, i.e., towards the reduced field of the diagram. Under strongly reduced conditions (i.e., at ΔFMQ−2 and in the DM675 sample), the ratio is lower than 1/3, thus indicating reducing fluids. The ratio becomes indicative of an oxidising fluid, even for a reduced carbonate metasedimentary composition, only above ~535 °C and ~2.14 GPa (Figure 6a). The shift from an oxidising to a reducing fluid shown by the X(O) ratio further proves the decoupled release of H_2^S and O_2^S under different redox conditions.

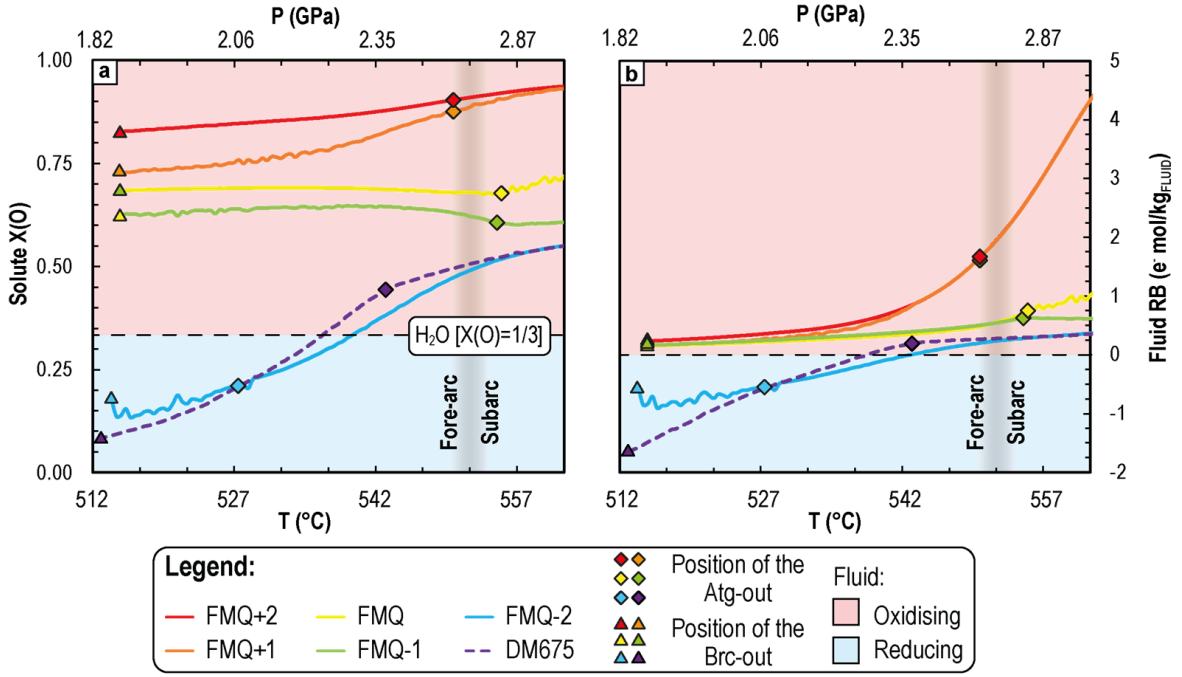

Figure 6. (**a**) Solute X(O) calculated as molar O_2^S/(O_2^S + H_2^S) and as a function of *T*, *P*, and fO_2. (**b**) Calculated redox budget of the modelled fluid as a function of *T*, *P*, and fO_2.

The fluid acidification, measured by the ΔpH during the entire antigorite dehydration, shows that the activity of the H^+ (aH^+) in the fluid increases with the progression of the reaction. This high aH^+ favours the protonation of the components of the system, i.e., the reactions between the dissociated H^+ in the fluid and the chemical elements within the minerals (e.g., $C + 4H^+ = CH_4$ or $FeS_2 + 4H^+ = 2H_2S + 2Fe_{solution/minerals}$). This protonation of the system's components due to increasing aH^+, together with the preferential release of H_2^S, suggests that $CaCO_3$-buffered antigorite dehydration is a reaction that favours the stabilisation of reduced species, such as CH_4 and H_2S.

5.2. Fluid Redox Budget

As previously explained, fO_2 is not an absolute variable and does not allow for a proper evaluation of the redox transfer capacity of the mobile phases (such as fluids) involved in redox processes across different rocks and environments (e.g., the transfer of the oxidising capacity from a subducting slab towards the overlying mantle wedge) [67]. Extensive variables, such as the redox budget (RB [60]), are preferable for evaluating the

redox capacity of a system (or fluid) in oxidising/reducing a reference system [60,65,69,70]. If we consider the redox transfer mediated by the fluids released from the subducting slab, the most important system that should be affected by this kind of process is the mantle wedge. The RB is the product of the amount of redox-sensitive elements and the number of electrons necessary to either oxidise or reduce a given element to another (reference) valence state [58]. For example, the C redox budget of 1 mol of CO_2 (C with a valence state of +4), in a subduction fluid interacting with a pristine mantle where graphite or diamond (i.e., C with a valence state of 0) can be stable, is calculated as follows:

$$\mathrm{RB}_{Fluid} = 1\ mol\ \mathrm{C}_{\mathrm{CO}_2} \times \left(+4^{\mathrm{CO}_2} - 0^{Gr/Dia}\right) = 1\ mol\ \mathrm{C} \times 4 = +4\ mol\ of\ \mathrm{RB}$$

To quantitatively evaluate the fluid redox transfer capacity, relative to a pre-subduction mantle, by using the specific redox budget parameter (see the Section 3 for definitions and calculation), the used reference state is that of a pristine mantle. The latter is reduced by 1-4 fO_2 log units relative to a mature and oxidised mantle wedge [1,2]. The considered redox-sensitive elements in the fluid and in the mantle are C, S, O, H, and Fe, and their mantle reference valence states are 0, −2, −2, +1, and +2, respectively. So, the specific redox budget of the fluid measures the moles of the electrons transferred, or not, by the fluid and added, or subtracted, to a pristine mantle wedge.

Due to the negligible abundance of dissolved Fe (Supplementary Figure S1) and the presence of dissolved O and H with a valence state other than −2 and +1, respectively, the contribution to the specific redox budget of these elements is completely negligible (being in the order of 10^{-4} mol e^-/kg_{fluid} for H_2 and in the order of 10^{-18} and 10^{-19} mol e^-/kg_{fluid} for Fe and O_2, respectively; see Supplementary Figure S2c–e) and is not treated further.

The specific redox budget calculated for a fluid produced during the carbonate-buffered breakdown of brucite and antigorite can have positive or negative values (Figure 6b). Positive specific redox budget values are indicative of a fluid characterised by an oxidising capacity relative to a pristine mantle. Negative specific redox budget values are indicative of a fluid characterised by a reducing capacity relative to a pristine mantle. Fluids belonging to the first case are those internally produced by a system at ΔFMQ-1 and above. Fluids belonging to the second group are those internally produced by a system at ΔFMQ-2 and by the DM675 sample below ~2.35 GPa and ~540 °C. Above such conditions, fluids equilibrated at ΔFMQ-2 and in the DM675 sample become slightly positive (Figure 6b).

In oxidised systems (i.e., at ΔFMQ+2 and ΔFMQ+1), carbonate and sulphate dissolution during antigorite breakdown can rise the specific redox budget only under *P-T* conditions close to those at which the reaction ends (Figure 6b). It is only under such conditions that carbonate and sulphate dissolution can more than double the oxidising capacity of the fluid in the span of about 10 °C (Figure 6b). In fluid internally produced by a system at FMQ or ΔFMQ-1, carbonates and pyrite dissolve during the entire rock's dehydration process, and the fluid specific redox budget retains small positive RB values (up to +0.75 mol e^-/kg_{fluid}; Figure 6b). Finally, for fluid internally produced by a system at ΔFMQ-2, the fluid's specific redox budget reduces after the brucite breakdown (Figure 6b). However, as soon as the antigorite is completely destabilised, the fluid's specific redox budget grows, reaching positive and oxidising values. The same trend is observed in the fluid produced by the DM675 sample, with the only difference being that the oxidising capacity is reached before the end of the antigorite breakdown. The general trend described by the redox budget under changing *P-T-*fO_2 conditions shows a dehydration process that stabilises either reducing or barely oxidising fluids. Only the concomitant dissolution of redox-sensitive minerals is able to shift the fluid redox state and capacity towards a substantial oxidising character.

5.3. $CaCO_3$+Antigorite Dehydration Reaction: Reducing or Oxidising?

The presented data indicate that the redox of the fluid produced during antigorite dehydration in an internally carbonate-buffered system (i.e., in a CM(F)S-COHS system) is ultimately imposed by the rock's redox state and by the redox-dependent dissolving minerals (Fe oxides, carbonates, graphite, sulphates, and sulphides). A similar conclusion has been proposed by Lazar [12] and by Evans and Frost [14] for antigorite dehydration in serpentinites. In the system investigated in the present paper, the small amount of Fe and the lack of Fe oxides imply that the redox state of the released fluids is influenced by both reacting (and dissolving) carbonates and dissolving S minerals. As the $CaCO_3$+antigorite dehydration reaction progresses to completion—independently from the system's redox state—(i) the preferential release of $H_2{}^S$ instead of $O_2{}^S$, (ii) the increase in aH^+, (iii) the increase in C and S valence states (i.e., they both start at lower values than those reached at the end of the reaction), and the progressive increase in the oxidising capacity of the fluid (as recorded by the fluid RB) highlight the contradictory aspect of the process. The reaction tends to produce a reducing fluid; however, the concomitant dissolution of redox-sensitive minerals (e.g., carbonates, graphite, sulphides, sulphates, and Fe oxides) supersedes this intrinsically reducing contribution to the fluid with, in the metacarbonate system, an overwhelmingly oxidising component. This reducing nature has also been suggested for antigorite dehydration in a carbonate-buffered system (i.e., in serpentinites) by, among others, Merkulova et al. [9] and Piccoli et al. [10]. However, the high redox-buffering capacity of the carbonatic system is testified by the increase in the fluid ΔpH after the end of antigorite dehydration and by the positive and oxidising redox budget acquired by the fluid during mineral dissolution, regardless of the fO_2 of the system. So, in metacarbonate sediments (potentially also for those with a higher metapelitic component), the H*P*-UH*P* dissolution of minerals by internally derived fluids, but also by externally derived ones, inevitably leads to the release of oxidising solute-bearing COHS fluids that are able to oxidise the overlying mantle wedge [71].

5.4. Linking Fluid Production Processes to Subduction Geodynamics

A recent experimental investigation of an ophicarbonate-like system (i.e., antigorite + 20 wt% of $CaCO_3$) highlighted how $CaCO_3$ depresses the *T* of antigorite-out compared to a $CaCO_3$-free serpentinite [15]. In such experiments, antigorite is consumed by 580 °C at 2.5 GPa, and even lower temperatures are predicted for increasing proportions of $CaCO_3$. This temperature is 100–150 °C lower than that predicted in a $CaCO_3$-free serpentinite [15]. Our thermodynamic modelling in a carbonate-dominated system (i.e., containing 80–90 wt% of $CaCO_3$) confirms the lower *T* for antigorite-out with respect to a carbonate-free system. At 1.8–2.8 GPa, antigorite-out is modelled between 518 and 555 °C, depending on the system's fO_2. These temperatures are similar to those obtained for dehydration in ophicarbonate systems (e.g., [72]).

To relate such observations to subduction geodynamics, the topologies of the α and β reactions were calculated in a *P-T* space in which the typical *P-T* paths of modern subduction zones were also reported [22] (Figure 7a). Reactions α and β were calculated for (i) the original (reduced) DM675 bulk composition, characterised by carbonate+graphite+ pyrite (representative of the DM675 bulk composition at ~ΔFMQ-2; cyan continuous curve, Figure 7a; Table 1); (ii) for an oxidised DM675 bulk composition, characterised by carbonate+ anhydrite (representative of the DM675 bulk composition at ~ΔFMQ+2; orange continuous curve, Figure 7a; Table 1); and (iii) for an average composition of hydrated abyssal peridotites [41]. In Figure 7a, it is possible to assess that, in a carbonate-dominated system, reaction α is exhausted at 30–70 °C higher than in a carbonate-free system, while reaction β is exhausted at 70–110 °C lower than in a carbonate-free system (Figure 7a). The insignificant gap of ~10–15 °C between the position of reaction β calculated for an oxidised and a reduced metacarbonate sediment suggests that, for modern subductions, fO_2 is less important than *T* and the bulk-rock composition (i.e., $CaCO_3$-free vs. $CaCO_3$-buffered systems). These differences in the reaction topology and in the location in the *P-T* space

and, especially in cold subduction regimes, the proximity between the brucite and the $CaCO_3$+antigorite dehydration reactions result in remarkable differences in the dynamics and duration of fluid release from typical serpentinites or from $CaCO_3$-dominated lithologies belonging to the CM(F)S-COHS system. In fact, the dehydration of carbonate-free serpentinites leads to continuous fluid production, as they are subducted at forearc depths; i.e., fluid release might occur in an interval of several km of depth and of ca. 200 °C. On the contrary, antigorite-bearing metacarbonate sediments/ophicarbonate should favour a "single" pulse of fluid production and release because it occurs in an interval of a few km of depth and of an interval of ca. 10–50 °C.

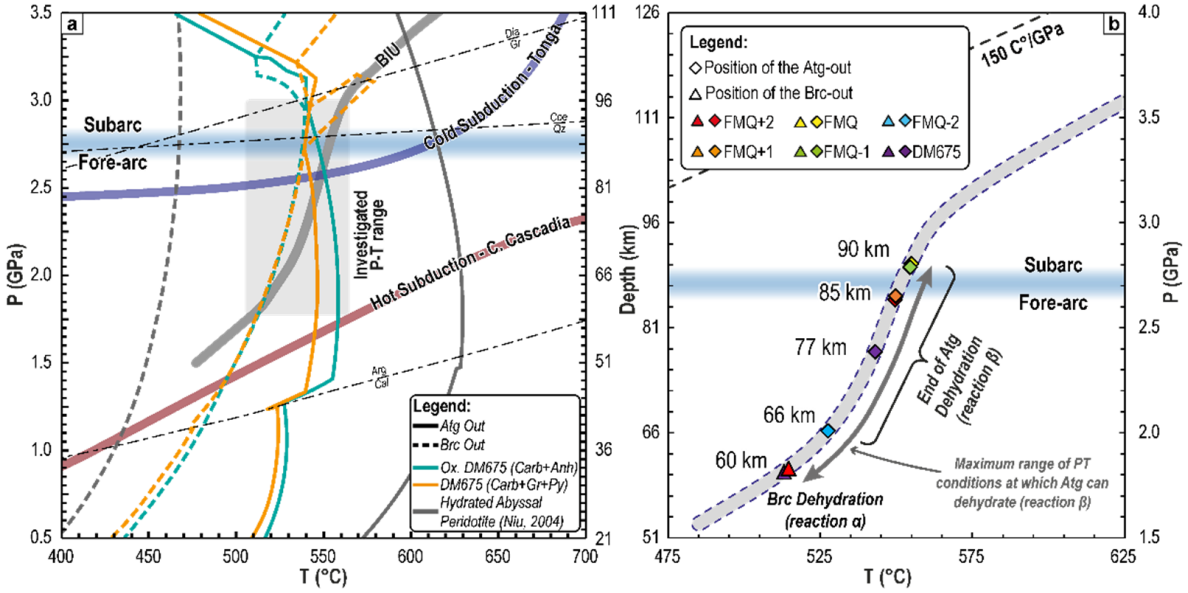

Figure 7. (**a**) *P-T* diagram showing topology and location of reactions α and β calculated for original (reduced) and modified (oxidised) DM675 bulk compositions and for the average composition of hydrated abyssal peridotites. (**b**) Location of brucite dehydration and end of $CaCO_3$-buffered antigorite dehydration as a function of fO_2 along the prograde BIU *P-T* path.

However, the type of *P-T* path followed by the subducting slab can amplify the role of fO_2 and *P* in regulating fluid production and release processes for a specific rock composition (Figure 7). In the case of Alpine-like cold subductions, the depth at which dolostone- or ophicarbonate-like lithologies start to release the highest amount of fluid is almost unaffected by the redox state of the system. Assuming lithostatic conditions, a 30 km thick upper plate [73] with an average density of 2750 kg/m^3, and a mantle wedge with a density of 3400 kg/m^3, brucite dehydration occurs at a ~60 km depth (Figure 7b) regardless of the redox state of the subducted rock. On the contrary, the depth at which these lithologies finish to produce fluids is influenced by the redox state of the system (Figure 7b). Following the same assumptions used above, fluid production ends at forearc depths between 66 and 77 km for strongly reduced lithologies (ΔFMQ-2–ΔFMQ-1.7), at subarc depths of ca. 90 km for reduced to slightly oxidised lithologies (ΔFMQ-1.8–ΔFMQ+0.7), and roughly at the transition from forearc to subarc settings (ca. 85 km) for more oxidised lithologies (>ΔFMQ+0.7).

Although modelled along a cold subduction *P-T* path, these results highlight the existence of a relationship between the geothermal gradient, the rock's redox state, and fluid production, which may also be present along hotter subduction *P-T* paths [12]. This heterogeneity in the duration of fluid release can continue within the subducting slab and can be paired with relevant differences in the chemical properties of the fluids released at distinct depths.

At forearc depths, reduced metasediments are more prone to produce fluids that are (i) richer in C and S, (ii) reducing or weakly oxidising, (iii) more acidic, due to the dissolution of carbonates, graphite, and pyrite. However, more oxidised sediments tend to release fluids that are (i) poorer in C and S, (ii) oxidising, and (iii) more alkaline, due to the dissolution of carbonates and either pyrite or sulphates.

If the metasedimentary system remains closed and fluid–rock re-equilibration—with the associated rock dissolution—persists to subarc depths, most of the fluid characteristics will be switched. Reduced metasediments will release fluids characterised by (i) a low S load, relative to that in oxidised metasediments, and a dissolved C that is lower than that at forearc depth, thus resulting in an overall lower total dissolved load; (ii) a weakly oxidising nature; and (iii) a higher pH, leading to a weaker acidic character. Finally, oxidised metasediments will release fluids characterised by (i) from two to six times more dissolved sulfur and a lower dissolved C, relative to fluids under reduced conditions, but with both being higher than fluids at forearc depths; (ii) from oxidising to strongly oxidising fluids; and (iii) heterogenous pH depending on the metasediments' redox state. These differences in fluid abundance, chemistry, and redox capacity might contribute to explaining the difference between an oxidised and fertile subarc mantle wedge [1,2] and an inert forearc mantle.

6. Conclusions

Integrating data obtained using electrolytic fluid thermodynamic models into redox budget calculations allows us to indirectly explore the interplay between redox processes and mineral dissolution in H*P*-UH*P* fluids [74,75]. In this work, we investigated and decoupled the intrinsic reducing nature of the carbonate-buffered antigorite dehydration reactions in metacarbonate sediments and the redox state and capacity of the released fluids as they were subsequently modified by mineral dissolution. During subduction, strongly reduced metacarbonates are likely able to release either reducing or weakly oxidising solute-bearing aqueous COHS fluids at forearc depths. However, weakly reduced to oxidised metacarbonates are likely to release weakly oxidising to strongly oxidising solute-bearing aqueous COHS fluids, respectively, at the transition between forearc and subarc depths. Our results indicate that, ultimately, dissolving redox-sensitive minerals will impose the redox state of the released fluid. Similar behaviour is also proposed for the fluids released by subducting serpentinites and could be suggested for the fluids released by ophicarbonates. This means that the weakly oxidising to strongly oxidising fluids released in systems ranging from (C)MFS-H_2O to CM(F)S-COHS are likely to metasomatise and oxidise the subarc mantle, thus recycling back C and S from the downgoing slab to the overlying mantle wedge and, then, into the arc crust and magmas. The associated volcanic degassing (both passive and explosive) of CO_2 and SO_2 (e.g., [76,77]) re-emits these climate-forcing gasses into the atmosphere. Finally, the solvent capacity of these fluids is responsible for the complexation and mobilisation of critical elements from the slab. These elements are concentrated in the arc crust though ore-forming processes (e.g., [3,4,61]), tracing the recycling pathways of the elements of economic interest.

Supplementary Materials: The following supporting information can be downloaded at https://www.mdpi.com/article/10.3390/geosciences13050130/s1, Figure S1: Dissolved Fe in the fluid phase as a function of *T*, *P,* and fO_2; Figure S2: Calculated specific redox budgets for C, S, O_2, H_2, and Fe as a function of *T*, *P,* and fO_2.

Author Contributions: Conceptualisation, A.M. and S.F.; methodology, AM. and J.A.D.C.; software, J.A.D.C.; validation, S.F., J.A.D.C., M.L.F. and D.C.; investigation, A.M.; data curation, A.M.; writing—original draft preparation, A.M.; writing—review and editing, A.M., S.F., J.A.D.C., M.L.F. and D.C.; visualisation, A.M.; supervision, S.F.; project administration, M.L.F. and S.F.; funding acquisition, M.L.F. and S.F. All authors have read and agreed to the published version of the manuscript.

Funding: This work was funded by the Italian Ministry of University and Research (PRIN 2017, Project n°: 2017LMNLAW to M.L.F.) and by the Università di Torino, "Fondo per la Ricerca Locale 2019–2020" to S.F.

Data Availability Statement: All the data necessary for reproducing the presented data are present in the manuscript.

Acknowledgments: Part of this paper is part of A.M.'s PhD thesis. The authors thank the three anonymous reviewers for their helpful comments that allowed for a previous version of the manuscript to be improved, clarified, and expanded. A.M. thanks Carosi R. for the invitation to contribute to this journal.

Conflicts of Interest: The authors declare no conflict of interest.

References

1. Wood, B.J.; Bryndzia, L.T.; Johnson, K.E. Mantle oxidation state and its relationship to tectonic environment and fluid speciation. *Science* **1990**, *248*, 337–345. [CrossRef] [PubMed]
2. Frost, D.J.; McCammon, C.A. The redox state of Earth's mantle. *Annu. Rev. Earth Planet. Sci.* **2008**, *36*, 389–420. [CrossRef]
3. Sun, W.; Huang, R.F.; Li, H.; Hu, Y.B.; Zhang, C.C.; Sun, S.J.; Zhang, L.P.; Ding, X.; Li, C.-Y.; Zartman, R.E.; et al. Porphyry deposits and oxidized magmas. *Ore Geol. Rev.* **2015**, *65*, 97–131. [CrossRef]
4. Chowdhury, P.; Dasgupta, R.; Phelps, P.R.; Costin, G.; Lee, C.T.A. Oxygen fugacity range of subducting crust inferred from fractionation of trace elements during fluid-present slab melting in the presence of anhydrite versus sulfide. *Geochim. Cosmochim. Acta* **2022**, *325*, 214–231. [CrossRef]
5. Bucher, K.; Grapes, R. *Petrogenesis of Metamorphic Rocks*; Springer Science & Business Media: Berlin/Heidelberg, Germany, 2011.
6. Peretti, A.; Dubessy, J.; Mullis, J.; Frost, B.R.; Trommsdorff, V. Highly reducing conditions during Alpine metamorphism of the Malenco peridotite (Sondrio, northern Italy) indicated by mineral paragenesis and H_2 in fluid inclusions. *Contrib. Mineral. Petrol.* **1992**, *112*, 329–340. [CrossRef]
7. Debret, B.; Andreani, M.; Muñoz, M.; Bolfan-Casanova, N.; Carlut, J.; Nicollet, C.; Schwartz, S.; Trcera, N. Evolution of Fe redox state in serpentine during subduction. *Earth Planet. Sci. Lett.* **2014**, *400*, 206–218. [CrossRef]
8. Debret, B.; Sverjensky, D.A. Highly oxidising fluids generated during serpentinite breakdown in subduction zones. *Sci. Rep.* **2017**, *7*, 10351. [CrossRef]
9. Merkulova, M.V.; Muñoz, M.; Brunet, F.; Vidal, O.; Hattori, K.; Vantelon, D.; Trcera, N.; Huthwelker, T. Experimental insight into redox transfer by iron-and sulfur-bearing serpentinite dehydration in subduction zones. *Earth Planet. Sci. Lett.* **2017**, *479*, 133–143. [CrossRef]
10. Piccoli, F.; Hermann, J.; Pettke, T.; Connolly JA, D.; Kempf, E.D.; Vieira Duarte, J.F. Subducting serpentinites release reduced, not oxidized, aqueous fluids. *Sci. Rep.* **2019**, *9*, 19573. [CrossRef]
11. Iacovino, K.; Guild, M.R.; Till, C.B. Aqueous fluids are effective oxidizing agents of the mantle in subduction zones. *Contrib. Mineral. Petrol.* **2020**, *175*, 36. [CrossRef]
12. Lazar, C. Using silica activity to model redox-dependent fluid compositions in serpentinites from 100 to 700 C and from 1 to 20 kbar. *J. Petrol.* **2020**, *61*, egaa101. [CrossRef]
13. Maurice, J.; Bolfan-Casanova, N.; Demouchy, S.; Chauvigne, P.; Schiavi, F.; Debret, B. The intrinsic nature of antigorite breakdown at 3 GPa: Experimental constraints on redox conditions of serpentinite dehydration in subduction zones. *Contrib. Mineral. Petrol.* **2020**, *175*, 94. [CrossRef]
14. Evans, K.A.; Frost, B.R. Deserpentinization in subduction zones as a source of oxidation in arcs: A reality check. *J. Petrol.* **2021**, *62*, 1–32. [CrossRef]
15. Eberhard, L.; Plümper, O.; Frost, D.J. Early release of H_2O during subduction of carbonated ultramafic lithologies. *Contrib. Mineral. Petrol.* **2023**, *178*, 17. [CrossRef]
16. Caurant, C.; Debret, B.; Ménez, B.; Nicollet, C.; Bouilhol, P. Redox heterogeneities in a subducting slab: Example from the Monviso meta-ophiolite (Western Alps, Italy). *Lithos* **2023**, *446–447*, 107136. [CrossRef]
17. Padrón-Navarta, J.A.; Sánchez-Vizcaíno, V.L.; Menzel, M.D.; Gómez-Pugnaire, M.T.; Garrido, C.J. Mantle wedge oxidation from deserpentinization modulated by sediment-derived fluids. *Nat. Geosci.* **2023**, *16*, 268–275. [CrossRef]
18. Ding, K.; Seyfried, W.E., Jr. Determination of Fe-Cl complexing in the low pressure supercritical region (NaCl fluid): Iron solubility constraints on pH of subseafloor hydrothermal fluids. *Geochim. Et Cosmochim. Acta* **1992**, *56*, 3681–3692. [CrossRef]
19. Yardley, B.W. 100th Anniversary Special Paper: Metal concentrations in crustal fluids and their relationship to ore formation. *Econ. Geol.* **2005**, *100*, 613–632. [CrossRef]
20. Ferrando, S.; Groppo, C.; Frezzotti, M.L.; Castelli, D.; Proyer, A. Dissolving dolomite in a stable UHP mineral assemblage: Evidence from Cal-Dol marbles of the Dora-Maira Massif (Italian Western Alps). *Am. Mineral.* **2017**, *102*, 42–60. [CrossRef]
21. Groppo, C.; Ferrando, S.; Gilio, M.; Botta, S.; Nosenzo, F.; Balestro, G.; Festa, A.; Rolfo, F. What's in the sandwich? New P–T constraints for the (U)HP nappe stack of southern Dora-Maira Massif (Western Alps). *Eur. J. Mineral.* **2019**, *31*, 665–683. [CrossRef]

22. Syracuse, E.M.; van Keken, P.E.; Abers, G.A. The global range of subduction zone thermal models. *Phys. Earth Planet. Inter.* **2010**, *183*, 73–90. [CrossRef]
23. Vialon, P. Etude Géologique du Massif Cristallin Dora-Maira: Alpes Cottiennes Internes: Italie. Doctoral Dissertation, Université de Grenoble, Grenoble, France, 1966.
24. Chopin, C. Coesite and pure pyrope in high-grade blueschists of the Western Alps: A first record and some consequences. *Contrib. Mineral. Petrol.* **1984**, *86*, 107–118. [CrossRef]
25. Compagnoni, R.; Rolfo, F.; Groppo, C.; Hirajima, T.; Turello, R. Geological map of the ultra-high pressure Brossasco-Isasca unit (Western Alps, Italy). *J. Maps* **2012**, *8*, 465–472. [CrossRef]
26. Maffeis, A.; Ferrando, S.; Connolly, J.A.; Groppo, C.; Frezzotti, M.L.; Castelli, D. Thermodynamic analysis of HP-UHP fluid inclusions: The solute load and chemistry of metamorphic fluids. *Geochim. Et Cosmochim. Acta* **2021**, *315*, 207–229. [CrossRef]
27. Compagnoni, R.; Borghi, A.; Cadoppi, P.; Ferrando, S.; Gattiglio, M.; Ruffini, R. The abundance of 47 elements and petrovolumetric models of the crust in the Susa Valley, Western Alps (Site 1). In *The Abundance of 55 Elements and Petrovolumetric Models of the Crust in 19 Type Areas from the Crystalline Basements of Italy, with Some Geophysical and Petrophysical Data*; Cesare, B., Mazzoli, C., Peruzzo, G., Rizzo, G., Sassi, R., Spiess, R., Eds.; Accademia Nazionale Delle Scienze Detta Dei XL: Roma, Italy, 2003; XXXII; pp. 69–96.
28. Bebout, G.E.; Agard, P.; Kobayashi, K.; Moriguti, T.; Nakamura, E. Devolatilization history and trace element mobility in deeply subducted sedimentary rocks: Evidence from Western Alps HP/UHP suites. *Chem. Geol.* **2013**, *342*, 1–20. [CrossRef]
29. Epstein, G.S.; Bebout, G.E.; Angiboust, S.; Agard, P. Scales of fluid-rock interaction and carbon mobility in the deeply underplated and HP-Metamorphosed Schistes Lustrés, Western Alps. *Lithos* **2020**, *354*, 105229. [CrossRef]
30. Epstein, G.S.; Bebout, G.E.; Angiboust, S. Fluid and mass transfer along transient subduction interfaces in a deep paleo-accretionary wedge (Western Alps). *Chem. Geol.* **2021**, *559*, 119920. [CrossRef]
31. Groppo, C.; Rapa, G.; Frezzotti, M.L.; Rolfo, F. The fate of calcareous pelites in collisional orogens. *J. Metamorph. Geol.* **2021**, *39*, 181–207. [CrossRef]
32. Plank, T. *The Chemical Composition of Subducting Sediments*; Elsevier: Amsterdam, The Netherlands, 2014.
33. Massonne, H.J. Phase relations of siliceous marbles at ultrahigh pressure based on thermodynamic calculations: Examples from the Kokchetav Massif, Kazakhstan and the Sulu terrane, China. *Geol. J.* **2011**, *46*, 114–125. [CrossRef]
34. Wang, S.J.; Teng, F.Z.; Li, S.G. Tracing carbonate–silicate interaction during subduction using magnesium and oxygen isotopes. *Nat. Commun.* **2014**, *5*, 5328. [CrossRef]
35. Tao, R.; Zhang, L.; Li, S.; Zhu, J.; Ke, S. Significant contrast in the Mg-CO isotopes of carbonate between carbonated eclogite and marble from the SW Tianshan UHP subduction zone: Evidence for two sources of recycled carbon. *Chem. Geol.* **2018**, *483*, 65–77. [CrossRef]
36. Zhang, K.J.; Li, Q.H.; Yan, L.L.; Zeng, L.; Lu, L.; Zhang, Y.X.; Hui, J.; Jin, X.; Tang, X.C. Geochemistry of limestones deposited in various plate tectonic settings. *Earth-Sci. Rev.* **2017**, *167*, 27–46. [CrossRef]
37. Farouk, S.; Ahmad, F.; Baioumy, H.; Lehmann, B.; Mohammed, I.Q.; Al-Kahtany, K. Geochemical characteristics of carbonaceous chalk near the Cretaceous/Paleogene transition, central Jordan: Strong metal enrichment of redox-sensitive and biophile elements from remineralized calcitic plankton. *Mar. Pet. Geol.* **2020**, *120*, 104535. [CrossRef]
38. Forshaw, J.B.; Pattison, D.R. Major-element geochemistry of pelites. *Geology* **2023**, *51*, 39–43. [CrossRef]
39. Cannaò, E.; Scambelluri, M.; Bebout, G.E.; Agostini, S.; Pettke, T.; Godard, M.; Crispini, L. Ophicarbonate evolution from seafloor to subduction and implications for deep-Earth C cycling. *Chem. Geol.* **2020**, *546*, 119626. [CrossRef]
40. Stucki, A. High Grade Mesozoic Ophiolites of the Southern Steep Belt, Central Alps. Doctoral Dissertation, ETH Zurich, Zurich, Switzerland, 2001.
41. Niu, Y. Bulk-rock major and trace element compositions of abyssal peridotites: Implications for mantle melting, melt extraction and post-melting processes beneath mid-ocean ridges. *J. Petrol.* **2004**, *45*, 2423–2458. [CrossRef]
42. Groppo, C.T.; Castelli, D.C.C.; Rolfo, F. HT, Pre-Alpine relics in a spinel-bearing dolomite marble from the UHP Brossasco-Isasca Unit (Dora-Maira Massif, western Alps). *Period. Di Mineral.* **2007**, *76*, 155–168.
43. Gebauer, D.H.P.S.; Schertl, H.P.; Brix, M.; Schreyer, W. 35 Ma old ultrahigh-pressure metamorphism and evidence for very rapid exhumation in the Dora Maira Massif, Western Alps. *Lithos* **1997**, *41*, 5–24. [CrossRef]
44. Ferrando, S.; Frezzotti, M.L.; Petrelli, M.; Compagnoni, R. Metasomatism of continental crust during subduction: The UHP whiteschists from the Southern Dora-Maira Massif (Italian Western Alps). *J. Metamorph. Geol.* **2009**, *27*, 739–756. [CrossRef]
45. Di Vincenzo, G.; Tonarini, S.; Lombardo, B.; Castelli, D.; Ottolini, L. Comparison of 40Ar–39Ar and Rb–Sr data on phengites from the UHP Brossasco–Isasca Unit (Dora Maira Massif, Italy): Implications for dating white mica. *J. Petrol.* **2006**, *47*, 1439–1465. [CrossRef]
46. Gauthiez-Putallaz, L.; Rubatto, D.; Hermann, J. Dating prograde fluid pulses during subduction by in situ U–Pb and oxygen isotope analysis. *Contrib. Mineral. Petrol.* **2016**, *171*, 15. [CrossRef]
47. Bonnet, G.; Chopin, C.; Locatelli, M.; Kylander-Clark, A.R.; Hacker, B.R. Protracted Subduction of the European Hyperextended Margin Revealed by Rutile U-Pb Geochronology Across the Dora-Maira Massif (Western Alps). *Tectonics* **2022**, *41*, e2021TC007170. [CrossRef]

48. Rubatto, D.; Hermann, J. Exhumation as fast as subduction? *Geology* **2001**, *29*, 3–6. [CrossRef]
49. Connolly, J.A. Computation of phase equilibria by linear programming: A tool for geodynamic modeling and its application to subduction zone decarbonation. *Earth Planet. Sci. Lett.* **2005**, *236*, 524–541. [CrossRef]
50. Connolly, J.A.; Galvez, M.E. Electrolytic fluid speciation by Gibbs energy minimization and implications for subduction zone mass transfer. *Earth Planet. Sci. Lett.* **2018**, *501*, 90–102. [CrossRef]
51. Holland TJ, B.; Powell, R. An improved and extended internally consistent thermodynamic dataset for phases of petrological interest, involving a new equation of state for solids. *J. Metamorph. Geol.* **2011**, *29*, 333–383. [CrossRef]
52. Sverjensky, D.A.; Harrison, B.; Azzolini, D. Water in the deep Earth: The dielectric constant and the solubilities of quartz and corundum to 60 kb and 1200 °C. *Geochim. Cosmochim. Acta* **2014**, *129*, 125–145. [CrossRef]
53. Pitzer, K.S.; Sterner, S.M. Equations of state valid continuously from zero to extreme pressures for H_2O and CO_2. *J. Chem. Phys.* **1994**, *101*, 3111–3116. [CrossRef]
54. de Santis, R.; Breedveld, G.J.F.; Prausnitz, J.M. Thermodynamic properties of aqueous gas mixtures at advanced pressures. *Ind. Eng. Chem. Process Des. Dev.* **1974**, *13*, 374–377. [CrossRef]
55. Holland, T.; Powell, R. Thermodynamics of order-disorder in minerals: II. Symmetric formalism applied to solid solutions. *Am. Mineral.* **1996**, *81*, 1425–1437. [CrossRef]
56. Padrón-Navarta, J.A.; Sánchez-Vizcaíno, V.L.; Hermann, J.; Connolly, J.A.; Garrido, C.J.; Gómez-Pugnaire, M.T.; Marchesi, C. Tschermak's substitution in antigorite and consequences for phase relations and water liberation in high-grade serpentinites. *Lithos* **2013**, *178*, 186–196. [CrossRef]
57. Evans, K.A.; Powell, R.; Holland, T.J.B. Internally consistent data for sulfur-bearing phases and application to the construction of pseudosections for mafic greenschist facies rocks in Na_2O-CaO-K_2O-FeO-MgO-Al_2O_3-SiO_2-CO_2-O-S-H_2O. *J. Metamorph. Geol.* **2010**, *28*, 667–687. [CrossRef]
58. Anovitz, L.M.; Essene, E.J. Phase equilibria in the system $CaCO_3$-$MgCO_3$-$FeCO_3$. *J. Petrol.* **1987**, *28*, 389–415. [CrossRef]
59. O'Neill, H.S. Quartz-fayalite-iron and quartz-fayalite-magnetite equilibria and the free energy of formation of fayalite (Fe_2SiO_4) and magnetite (Fe_3O_4). *Am. Mineral.* **1987**, *72*, 67–75.
60. Evans, K.A. Redox decoupling and redox budgets: Conceptual tools for the study of earth systems. *Geology* **2006**, *34*, 489–492. [CrossRef]
61. Tomkins, A.G.; Evans, K.A. Separate zones of sulfate and sulfide release from subducted mafic oceanic crust. *Earth Planet. Sci. Lett.* **2015**, *428*, 73–83. [CrossRef]
62. Whitney, D.L.; Evans, B.W. Abbreviations for names of rock-forming minerals. *Am. Mineral.* **2010**, *95*, 185–187. [CrossRef]
63. Frezzotti, M.L.; Ferrando, S. The chemical behavior of fluids released during deep subduction based on fluid inclusions. *Am. Mineral.* **2015**, *100*, 352–377. [CrossRef]
64. Ferrando, S.; Petrelli, M.; Frezzotti, M.L. Gradual and selective trace-element enrichment in slab-released fluids at sub-arc depths. *Sci. Rep.* **2019**, *9*, 16393. [CrossRef]
65. Connolly, J.A.D. Phase diagram methods for graphitic rocks and application to the system C-O-H-FeO-Eo-$_2$-eO-$_2$. *Contrib. Mineral. Petrol.* **1995**, *119*, 94–116. [CrossRef]
66. Galvez, M.E.; Connolly, J.A.; Manning, C.E. Implications for metal and volatile cycles from the pH of subduction zone fluids. *Nature* **2016**, *539*, 420–424. [CrossRef] [PubMed]
67. Sverjensky, D.A. Thermodynamic modelling of fluids from surficial to mantle conditions. *J. Geol. Soc.* **2019**, *176*, 348–374. [CrossRef]
68. Galvez, M.E.; Manning, C.E.; Connolly, J.A.; Rumble, D. The solubility of rocks in metamorphic fluids: A model for rock-dominated conditions to upper mantle pressure and temperature. *Earth Planet. Sci. Lett.* **2015**, *430*, 486–498. [CrossRef]
69. Galvez, M.E.; Jaccard, S.L. Redox capacity of rocks and sediments by high temperature chalcometric titration. *Chem. Geol.* **2021**, *564*, 120016. [CrossRef]
70. Tumiati, S.; Malaspina, N. Redox processes and the role of carbon-bearing volatiles from the slab–mantle interface to the mantle wedge. *J. Geol. Soc.* **2019**, *176*, 388–397. [CrossRef]
71. Ague, J.J.; Tassara, S.; Holycross, M.E.; Li, J.L.; Cottrell, E.; Schwarzenbach, E.M.; Fassoulas, C.; John, T. Slab-derived devolatilization fluids oxidized by subducted metasedimentary rocks. *Nat. Geosci.* **2022**, *15*, 320–326. [CrossRef]
72. Menzel, M.D.; Garrido, C.J.; López Sánchez-Vizcaíno, V.; Hidas, K.; Marchesi, C. Subduction metamorphism of serpentinite-hosted carbonates beyond antigorite-serpentinite dehydration (Nevado-Filábride Complex, Spain). *J. Metamorph. Geol.* **2019**, *37*, 681–715. [CrossRef]
73. Malusà, M.G.; Guillot, S.; Zhao, L.; Paul, A.; Solarino, S.; Dumont, T.; Schwartz, S.; Aubert, C.; Baccheschi, P.; Eva, E.; et al. The deep structure of the Alps based on the CIFALPS seismic experiment: A synthesis. *Geochem. Geophys. Geosystems* **2021**, *22*, e2020GC009466. [CrossRef]
74. Duan, W.Y.; Li, X.P.; Schertl, H.P.; Willner, A.P. COHS fluids released by oceanic serpentinite in subduction zones: Implications for arc-magma oxidation. *Earth Planet. Sci. Lett.* **2022**, *594*, 117709. [CrossRef]
75. Li, Y.B.; Chen, Y.; Su, B.; Zhang, Q.H.; Shi, K.H. Redox species and oxygen fugacity of slab-derived fluids: Implications for mantle oxidation and deep carbon-sulfur cycling. *Front. Earth Sci.* **2022**, *10*, 1–13. [CrossRef]

76. Fischer, T.P.; Arellano, S.; Carn, S.; Aiuppa, A.; Galle, B.; Allard, P.; Lopez, T.; Shinohara, H.; Kelly, P.; Werner, C.; et al. The emissions of CO_2 and other volatiles from the world's subaerial volcanoes. *Sci. Rep.* **2019**, *9*, 18716. [CrossRef] [PubMed]
77. Carn, S.A.; Fioletov, V.E.; McLinden, C.A.; Li, C.; Krotkov, N.A. A decade of global volcanic SO_2 emissions measured from space. *Sci. Rep.* **2017**, *7*, 44095. [CrossRef] [PubMed]